The Astrophysical Journal, 785:121 (9pp), 2014 April 20 doi:10.1088/0004-637X/785/2/121

REVEALING THE NATURE OF THE ULX AND X-RAY POPULATION OF THE SPIRAL GALAXY NGC 4088

M. Mezcua[1,2], G. Fabbiano[3], J. C. Gladstone[4], S. A. Farrell[5], and R. Soria[6]
[1] Instituto de Astrofísica de Canarias (IAC), E-38200 La Laguna, Tenerife, Spain; mmezcua@iac.es
[2] Universidad de La Laguna, Department Astrofísica, E-38206 La Laguna, Tenerife, Spain
[3] Harvard-Smithsonian Center for Astrophysics (CfA), 60 Garden Street, Cambridge, MA 02138, USA
[4] Department of Physics, University of Alberta, 11322-89 Avenue, Edmonton, Alberta T6G 2G7, Canada
[5] Sydney Institute for Astronomy (SIfA), School of Physics, The University of Sydney, NSW 2006, Australia
[6] International Centre for Radio Astronomy Research, Curtin University, GPO Box U1987, Perth, WA 6845, Australia
Received 2013 November 18; accepted 2014 March 3; published 2014 April 2

ABSTRACT

We present the first *Chandra* and *Swift* X-ray study of the spiral galaxy NGC 4088 and its ultraluminous X-ray source (ULX N4088–X1). We also report very long baseline interferometry (VLBI) observations at 1.6 and 5 GHz performed quasi-simultaneously with the *Swift* and *Chandra* observations, respectively. Fifteen X-ray sources are detected by *Chandra* within the D25 ellipse of NGC 4088, from which we derive the X-ray luminosity function (XLF) of this galaxy. We find the XLF is very similar to those of star-forming galaxies and estimate a star-formation rate of 4.5 $M_{\odot}$ yr^{-1}. The *Chandra* detection of the ULX yields its most accurate X-ray position, which is spatially coincident with compact radio emission at 1.6 GHz. The ULX *Chandra* X-ray luminosity, $L_{0.2-10.0\,\mathrm{keV}} = 3.4 \times 10^{39}$ erg s^{-1}, indicates that N4088–X1 could be located at the high-luminosity end of the high-mass X-ray binary (HMXB) population of NGC 4088. The estimates of the black hole (BH) mass and ratio of radio to X-ray luminosity of N4088–X1 rule out a supermassive BH nature. The *Swift* X-ray spectrum of N4088–X1 is best described by a thermal Comptonization model and presents a statistically significant high-energy cutoff. We conclude that N4088–X1 is most likely a stellar remnant BH in an HMXB, probably fed by Roche lobe overflow, residing in a super-Eddington ultraluminous state. The 1.6 GHz VLBI source is consistent with radio emission from possible ballistic jet ejections in this state.

Key words: accretion, accretion disks – black hole physics – ISM: jets and outflows – radio continuum: general – X-rays: binaries

Online-only material: color figures

1. INTRODUCTION

Early X-ray observations of nearby galaxies with the *Einstein Observatory*, and later with *ROSAT*, *ASCA*, *XMM-Newton*, and *Chandra*, revealed the presence of a population of off-nuclear X-ray point sources with X-ray luminosities above the Eddington limit for a stellar-mass black hole (BH; $L_{\mathrm{X}} > 10^{39}$ erg s^{-1}; Fabbiano 1989). These high luminosities imply BHs of masses $>10\,M_{\odot}$, if the accretion is sub-Eddington and the radiation is isotropic. This suggested that ULXs could be intermediate mass BHs (IMBHs) with BH masses in the range $100 \leqslant M_{\mathrm{BH}} \leqslant 10^{5}\,M_{\odot}$ (e.g., Colbert & Mushotzky 1999). The alternative is stellar-remnant BHs ($M_{\mathrm{BH}} < 100\,M_{\odot}$) accreting around or above the Eddington limit (e.g., King et al. 2001; Fabbiano 2005; Feng & Soria 2011).

Studies of the X-ray luminosity function (XLF) of the X-ray populations of these nearby galaxies are a very useful tool for discerning between different types of X-ray populations and galaxy properties (e.g., morphological type, age of stellar population) and investigating the nature of the X-ray sources that populate them (e.g., X-ray binaries-XRBs; see review by Fabbiano 2006). The XLF of late-type star-forming galaxies is usually described by a straight power law and is associated with a population of high-mass X-ray binaries (HMXBs) located in regions of star formation (e.g., Zezas & Fabbiano 2002; Colbert et al. 2004; Zezas et al. 2007). Early-type galaxies are best described by an XLF with a broken power law and a break at a few times 10^{38} erg s^{-1} (attributed to the Eddington luminosity of neutron star XRBs; e.g., Sarazin et al. 2000, 2001), and are thought to be dominated by a population of low-mass XRBs (LMXBs, e.g., Kim & Fabbiano 2004, 2010; Gilfanov 2004). Studies on the XLF of different galaxies can also be used to gain insight into the nature of ULXs.

ULX population studies have revealed that many ULXs are associated with young star-forming regions and star-forming galaxies (e.g., Swartz et al. 2004, 2009). They also tend to be found in low-metallicity regions (e.g., Zampieri & Roberts 2009; Belczynski et al. 2010; Mapelli et al. 2010). Such low metallicities are required in order to make more massive BHs (e.g., Heger et al. 2003), which shows that it would be possible for ULXs to be massive stellar remnant BHs. However, population studies of the HMXB population of the local universe have also revealed an unbroken power-law slope in the XLF up to $\sim 2 \times 10^{40}$ erg s^{-1} (e.g., Grimm et al. 2003; Swartz et al. 2011; Mineo et al. 2012). This continuation indicates that the majority of ULXs with $L_{\mathrm{X}} < 2 \times 10^{40}$ erg s^{-1} are likely to be HMXBs with a stellar-mass BH accreting around or above the Eddington limit.

Many studies have been undertaken to obtain the mass of the putative BH contained in ULXs. Such methods include: studying the ULX optical counterpart (e.g., Pakull et al. 2006; Kaaret & Corbel 2009; Cseh et al. 2011; Tao et al. 2011; Gladstone et al. 2013); or X-ray analysis, using either spectral fitting (e.g., Miller et al. 2003; Gladstone & Roberts 2009; Caballero-García & Fabian 2010; Davis et al. 2011; Godet et al. 2012; Bachetti et al. 2013), the luminosity–temperature relation (e.g., Miller et al. 2003; Gladstone & Roberts 2009; Strateva & Komossa 2009; Servillat et al. 2011), quasi-periodic oscillations (e.g., Strohmayer & Mushotzky 2003; Strohmayer et al. 2007; Caballero-García et al. 2013), or X-ray variability

(Soria et al. 2004; Heil et al. 2009; De Marco et al. 2013). In those cases where candidate radio counterparts have been identified, attempts have been made to obtain the BH mass using the Fundamental Plane of accreting BHs (e.g., Sánchez-Sutil et al. 2006; Cseh et al. 2011; Mezcua & Lobanov 2011; Webb et al. 2012; Mezcua et al. 2013a, 2013c). The Fundamental Plane is a correlation between 2–10 keV X-ray luminosity, 5 GHz radio luminosity, and BH mass that holds for sub-Eddington accreting BHs in the low/hard X-ray state and with steady jet emission (e.g., Merloni et al. 2003; Körding et al. 2006; Gallo et al. 2012). The detection of compact core radio emission is required in order to locate a ULX in the Fundamental Plane, which can be achieved only by means of very long baseline interferometry (VLBI) radio observations. Mezcua & Lobanov (2011) initiated a program with the European VLBI Network (EVN[7]) aimed at detecting and studying the milliarcsecond-scale emission of ULXs. Such investigations have indicated that those ULXs with radio counterparts may be powered by IMBHs (e.g., Mezcua & Lobanov 2011; Mezcua et al. 2013a, 2013c). Here, we investigate one of these ULXs in NGC 4088.

NGC 4088 is an asymmetric spiral galaxy ($D_{\rm L}$ = 13 Mpc, redshift = 0.002524; Verheijen & Sancisi 2001) hosting a ULX (N4088–X1) offset ∼32 arcsec from the nucleus. N4088–X1 was first detected with the *ROSAT* satellite by Liu & Bregman (2005), who reported an X-ray luminosity $L_{0.3-8.0\,\rm keV} \sim 6 \times 10^{39}$ erg s^{-1}. The ULX is located within the spiral arm of NGC 4088, possibly within an H II region (e.g., Liu & Bregman 2005; Sánchez-Sutil et al. 2006). A cross-match of the Very Large Array (VLA[8]) FIRST[9] catalog with *ROSAT* ULX catalogs (e.g., Liu & Bregman 2005) revealed a 1.4 GHz VLA radio counterpart for the ULX of 1.87 mJy, with an offset between the *ROSAT* and the radio position of 3.6 arcsec (Sánchez-Sutil et al. 2006). Later EVN observations at 1.6 GHz yielded the detection of a compact, unresolved component of 0.1 mJy centered at R.A.(J2000) = $12^{\rm h}05^{\rm m}31\overset{\rm s}{.}7110 \pm 0\overset{\rm s}{.}0003$, decl.(J2000) = $50^\circ32'46\overset{''}{.}729 \pm 0\overset{''}{.}002$ (Mezcua & Lobanov 2011). This provided an upper limit on the 5 GHz luminosity (assuming a radio spectral index $\alpha = 0.15$), from which an upper limit on the ULX BH mass of $\sim 10^5\ M_\odot$ was estimated using the Fundamental Plane of accretion (Mezcua & Lobanov 2011).

In this paper, we present the first *Chandra* observations of the galaxy NGC 4088 and the ULX N4088–X1, as well as quasi-simultaneous VLBI observations with the EVN at 5 GHz. We also report a reanalysis of the EVN data at 1.6 GHz, now imaged at the *Chandra* position reported in this paper, and the analysis of 23 *Swift* observations performed nearly at the same time (between 2009 April and September) as the 1.6 GHz EVN observations (2009 June 1–2). With these data we investigate the proposed association between the X-ray and radio emission (for which a sub-arcsecond X-ray position is needed) of N4088–X1 and attempt to estimate the BH mass with the aim of revealing the nature of this ULX.

The paper is organized as follows. The observations and data analysis are presented in Section 2, while the main results obtained are shown in Section 3 and discussed in Section 4. Final conclusions are presented in Section 5.

Through this paper, we assume a ΛCDM cosmology with parameters $H_0 = 73$ km s^{-1} Mpc^{-1}, $\Omega_\Lambda = 0.73$, and $\Omega_{\rm m} = 0.27$.

[7] www.evlbi.org
[8] Very Large Array of the National Radio Astronomy Observatory (NRAO).
[9] Faint Images of the Radio Sky at Twenty-cm survey.

2. OBSERVATIONS AND DATA ANALYSIS

2.1. Chandra X-Ray Observations

The ULX N4088–X1 was observed on 2012 June 6 (Obs. ID: 14442; PI: Mezcua) with the *Chandra X-ray observatory* (Weisskopf et al. 2002). The observation was performed using the Advanced CCD Imaging Spectrometer (ACIS) detector (Garmire 1997) with an integration time of 19.8 ks. The data were reprocessed using CIAO version 4.5 and the corresponding calibration files, following the standard *Chandra* ACIS data analysis threads.[10] The *chandra_repro* reprocessing script was used to reprocess the data and generate a new level=2 event file.

An image of the S3 chip (ccd_id=7), a background image, and a PSF map that provides the size of the point spread function (PSF) at each pixel in the image were then produced using the tools *dmcopy*, *aconvolve*, and *mkpsfmap* and given to *wavdetect*, which performed source detection and extracted source net counts in the energy range 0.3–10 keV. The detected source count rates for all sources lying within the D25 ellipse of NGC 4088 were converted to source fluxes by applying a conversion factor calculated assuming a power-law spectrum of $\Gamma = 1.8$ and line-of-sight Galactic absorption[11] $N_{\rm H} = 2 \times 10^{20}$ cm^{-2} using WebPIMMS.[12] A $\Gamma = 1.4 \sim 2$ (e.g., Zezas & Fabbiano 2002) and $\Gamma = 1.4$–1.8 (e.g., Boroson et al. 2011) was found for HMXBs and LMXBs, respectively. We note that the average value of $\Gamma = 1.8$ used here may not be applicable to our case since those studies have a deeper detection limit that includes also XRBs in the low/hard state (dominated by a hard power-law component), while we can only see those in the high/soft state (dominated by a disk blackbody). To make sure that we are using a plausible slope, we used the XSPEC task *fakeit* to simulate a distribution of *Chandra* spectra for disk-blackbody models with column densities equal to the line of sight and twice the line-of-sight values, and inner-disk temperatures distributed between 0.6 and 1.0 keV (typical disk temperatures in the high/soft state; e.g., McClintock & Remillard 2006). We then re-fitted the simulated spectra with a power-law model, fixing the column density to the line-of-sight value and leaving the photon index as a free parameter. We find that low signal-to-noise (S/N) disk-blackbody spectra in that temperature range are indeed approximated in the *Chandra* band (at least for the purpose of converting from count rates to fluxes) by power laws of photon index between ∼1.5 (for $T_{\rm in} \sim 1$ keV) and ∼2 (for $T_{\rm in} \sim 0.6$ keV), with the most likely value $\Gamma \sim 1.8$.

The source spectrum of N4088–X1 was extracted using the *specextract* script and selecting a circular region of 2″ around the target source and of 15″ in a source-free area of the same chip for the background. The extracted spectrum was grouped to 15 counts per energy bin to allow for χ^2 fitting using the tool *grppha*.

2.2. Swift X-Ray Observations

NGC 4088 was observed on 23 occasions in X-rays with the *Swift* X-ray Telescope (XRT) between 2009 April 15 and 2009 September 21 as part of a monitoring campaign targeting the supernova (SN) SN2009dd (see Table 1 for a log of the *Swift* observations). We generated images, light curves, and spectra, including the background and ancillary response files, with the

[10] http://cxc.harvard.edu/ciao/threads/
[11] $N_{\rm H}$ calculated using the COLDEN tool: http://cxc.harvard.edu/toolkit/colden.jsp.
[12] http://heasarc.nasa.gov/Tools/w3pimms.html

Table 1
Log of the *Swift* XRT Observations of N4088–X1

Date	ObsID	Exp. Time (s)	Spectrum
2009 Apr 15	00031401001	1996	Y
2009 Apr 17	00031401002	830	Y
2009 Apr 19	00031401003	3946	Y
2009 Apr 21	00031401004	2670	Y
2009 Apr 25	00031401005	2712	Y
2009 May 10	00031401006	4306	Y
2009 May 16	00031401007	6045	Y
2009 Jul 4	00031401008	3824	Y
2009 Jul 5	00031401009	5957	Y
2009 Jul 15	00031401011	3930	N
2009 Jul 16	00031401012	8963	N
2009 Jul 19	00031401013	4863	Y
2009 Jul 19	00031401014	6049	N
2009 Jul 26	00031401015	4668	N
2009 Jul 27	00031401016	5181	N
2009 Aug 2	00031401017	5934	Y
2009 Aug 3	00031401018	4647	Y
2009 Aug 9	00031401019	6968	Y
2009 Sep 13	00031401020	33	Y
2009 Sep 14	00031401021	4593	Y
2009 Sep 16	00031401022	4587	Y
2009 Sep 20	00031401023	5858	Y
2009 Sep 21	00031401024	6135	Y

Note. The observations used for producing the combined spectrum are indicated in Column 4.

online XRT data product generator[13] (Evans et al. 2009). We downloaded suitable spectral response files for single and double events in photon-counting mode from the latest calibration database. N4088–X1 was clearly detected in all observations with an average XRT count rate of 0.0037 count s^{-1}. We extracted a light curve binned at the duration of each individual observation, finding evidence for small deviations from the average count rate in 5 of the 23 observations, though no evidence for significant spectral variability could be seen in the standard Swift hardness ratio ((1.5–10 keV)/(0.3–1.5 keV)). We next extracted a combined spectrum from the *Chandra* position of N4088–X1, excluding the 5 observations in which evidence for variability was seen, giving a total exposure time of 76 ks.

2.3. VLBI Radio Observations

N4088–X1 was observed with the EVN at 5 GHz on 2012 June 1 (project code: EM095A; PI: Mezcua). Eight antennas participated in the observations: Effelsberg (Germany), Westerbork (The Netherlands), Jodrell Bank (United Kingdom), Onsala (Sweden), Medicina (Italy), Noto (Italy), Torun (Poland), and Yebes (Spain). The observations were performed using the phase-referencing technique, in which the target and a nearby, compact, bright source (the phase calibrator) are observed interleaving scans. A target-phase calibrator cycle of four minutes (three minutes on the target, one minute on the phase calibrator) was used. As a result, a total of 2.7 hr was spent on the target source. The source J1203+4803 was used as phase calibrator, while the bright and compact radio source 4C+39.25 was used as fringe finder and bandpass calibrator.

The data were recorded in dual-circular polarization and at sample rate of 1024 megabit per second (Mbps). Eight intermediate frequency bands, each of 16 MHz each and 32 spectral channels, were used. The data correlation was performed at JIVE[14] with an averaging time of 4 s.

The calibration of the correlated data was performed using AIPS.[15] Amplitudes were calibrated using the gains of the antennas and system temperatures. The data were then fringe-fitted using the phase calibrator. Delay, delay rate, and phase solutions derived from the phase calibrator were interpolated and applied to the target. The imaging was performed using CLEAN deconvolution with the AIPS task IMAGR. Natural weighting images were produced from non-channel-averaged data[16] and imaging two fields of view (FOV) derived from the positional errors of the VLA and *Chandra* ULX counterparts: one of $\sim 1 \times 1$ arcsec^2 centered at the *Chandra* position, and another one of $\sim 5 \times 5$ arcsec^2 centered at the VLA position. The restoring beam size was 5.7 mas $\times$ 4.5 mas. To enhance the sensitivity, we also repeated the multi-field imaging without using the baselines longer than 20 Mλ.

We did also recalibrate the 1.6 GHz EVN data previous analyzed by Mezcua & Lobanov (2011) and reimaged the data without averaging the channels and using the same two FOVs as at 5 GHz. The imaging was also performed using only the baselines shorter than 15 Mλ, which resulted in a beam size of 33 mas $\times$ 27 mas.

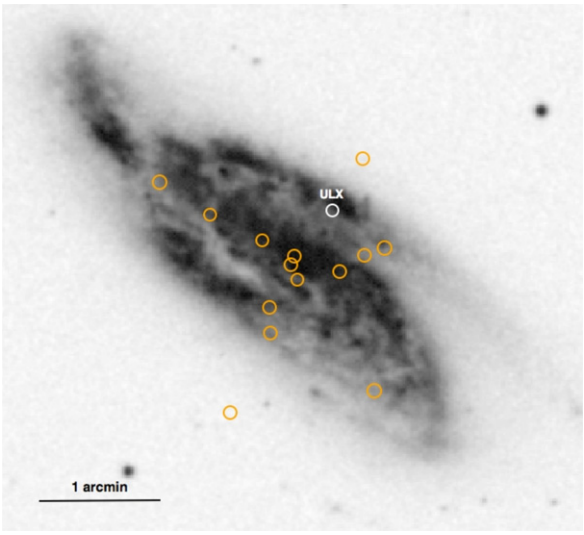

Figure 1. Digitized Sky Survey (Lasker et al. 1990) image of NGC 4088. The position of the 15 sources detected by *wavdetect* in the 0.3–10 keV band within the D25 ellipse of NGC 4088 are marked with orange circles of radius 3 arcsec. The position of the ULX is marked with a white circle.
(A color version of this figure is available in the online journal.)

3. RESULTS

A total of 31 X-ray sources are detected by *wavdetect* in the 0.3–10 keV band, of which 15 lay within the D25 ellipse of the host galaxy. The location of the 15 detected sources is shown in Figure 1, and their position, observed flux, and 0.3–10 keV band luminosity are provided in Table 2.

[13] www.swift.ac.uk/user_objects/

[14] Joint Institute for VLBI in Europe, Dwingeloo, the Netherlands.

[15] Astronomical Image Processing Software of NRAO.

[16] No channel averaging was applied to the calibrated data to avoid degradation of the synthesized beam away from the phase center (bandwidth smearing).

Table 2
Point-like *Chandra* X-Ray Sources Detected in the 0.3–10 keV Band Inside the D25 Ellipse of NGC 4088

Source	R.A. (J2000)	decl. (J2000)	Net Counts	$L_{0.3-10\,\mathrm{keV}}$ ($\times 10^{38}$ erg s^{-1})
N4088–X1	12 05 32.33 ± 0.01	50 32 45.9 ± 0.1	221.2 ± 15.3	21.9 ± 1.5
Src. 2	12 05 29.73 ± 0.01	50 32 28.3 ± 0.1	89.1 ± 9.8	8.8 ± 1.0
Src. 3	12 05 31.92 ± 0.01	50 32 16.9 ± 0.2	60.5 ± 8.3	6.0 ± 0.8
Src. 4[a]	12 05 34.36 ± 0.02	50 32 19.9 ± 0.2	49.3 ± 7.8	4.9 ± 0.8
Src. 5	12 05 35.41 ± 0.01	50 31 59.7 ± 0.1	49.3 ± 7.4	4.9 ± 0.7
Src. 6	12 05 30.70 ± 0.02	50 32 24.9 ± 0.2	47.3 ± 7.4	4.7 ± 0.7
Src. 7	12 05 34.18 ± 0.01	50 32 24.3 ± 0.1	27.6 ± 6.1	2.7 ± 0.6
Src. 8	12 05 35.34 ± 0.00	50 31 47.6 ± 0.1	22.8 ± 5.1	2.3 ± 0.5
Src. 9	12 05 30.83 ± 0.02	50 33 10.8 ± 0.2	20.3 ± 4.8	2.0 ± 0.5
Src. 10	12 05 38.40 ± 0.01	50 32 43.2 ± 0.1	17.1 ± 4.5	1.7 ± 0.4
Src. 11	12 05 37.29 ± 0.02	50 31 09.4 ± 0.4	15.1 ± 4.4	1.5 ± 0.4
Src. 12	12 05 40.92 ± 0.05	50 32 58.6 ± 0.3	13.9 ± 4.4	1.4 ± 0.4
Src. 13	12 05 35.80 ± 0.03	50 32 31.4 ± 0.3	11.6 ± 4.1	1.2 ± 0.4
Src. 14	12 05 34.02 ± 0.01	50 32 12.9 ± 0.2	8.2 ± 3.5	0.8 ± 0.3
Src. 15	12 05 30.13 ± 0.04	50 31 21.0 ± 0.2	8.0 ± 3.2	0.8 ± 0.3
SN2009dd[b]	12 05 34.10	50 32 19.4	8.0 ± 3.2	0.8 ± 0.3

Notes. Fluxes and luminosities are unabsorbed, derived assuming $\Gamma = 1.8$ and line-of-sight Galactic column density $N_{\mathrm{H}} = 2 \times 10^{20}$ cm^{-2}. The positional 1σ errors reported correspond to the statistical uncertainties from the PSF fitting performed by *wavdetect*. A systematic pointing error of up to 0.6 arcsec can also affect the *Chandra* absolute astrometry.
[a] Src. 4 is the most probable nucleus of NGC 4088.
[b] Not detected by *wavdetect*, counts obtained from CIAO statistics.

3.1. X-Ray Properties of the ULX

For the ULX N4088–X1, we obtain an X-ray luminosity of $L_{0.3-10\,\mathrm{keV}} = 2.2 \times 10^{39}$ erg s^{-1} using the observed *Chandra* fluxes derived from the count rates assuming the power-law model described in Section 2.1. The *Chandra* detection of N4088–X1 shows that the source is located at R.A.(J2000) = $12^{\mathrm{h}}05^{\mathrm{m}}32\overset{\mathrm{s}}{.}33 \pm 0\overset{\mathrm{s}}{.}01$, decl.(J2000) = $50^{\circ}32'45\overset{''}{.}9 \pm 0\overset{''}{.}1$. The positional 1σ errors correspond to the statistical uncertainties affecting the *wavdetect* centroid algorithm and the dispersion of photons due to the PSF. In addition, the *Chandra* absolute astrometry can be shifted by up to 0.6 arcsec due to pointing uncertainties.

3.1.1. Chandra ULX Spectral Modeling

We fitted the *Chandra* spectrum using the X-ray spectral fitting package XSPEC (Arnaud 1996) v12.7.1 in the 0.2–10.0 keV energy range. Two models were used: an absorbed multicolor disk-blackbody model (*wabs*diskbb*) and a power-law model (*wabs*pow*). The fits were performed using the minimum χ^2 method (i.e., Gehrels Chisq statistics). The fitting results of each model are shown in Table 3, while a plot of the power-law spectral fit is shown in Figure 2.

Both the *pow* and the *diskbb* model provide acceptable statistical fits (i.e., null-hypothesis probability >5%, so rejection likelihood <95%), with values of $N_{\mathrm{H}} \sim 10$–15 times larger than the Galactic column density (i.e., $N_{\mathrm{H}} = 2 \times 10^{20}$ cm^{-2}; Kalberla 2003). The data are insufficient to statistically distinguish between models. The disk-blackbody model provides an inner disk temperature $kT_{\mathrm{in}} = 2.5$ keV, too high for a standard disk. The power-law fit provides a very hard photon index $\Gamma = 1.1$ and unabsorbed flux $= 1.7 \times 10^{-13}$ erg s^{-1} cm^2, from which we derive an X-ray luminosity $L_{0.2-10.0\,\mathrm{keV}} = 3.4 \times 10^{39}$ erg s^{-1}.

3.1.2. Swift ULX Spectral Modeling

We fitted the co-added *Swift* spectrum using XSPEC again, with an absorbed power-law model with absorption accounted for using the *wabs* model and the N_{H} column set to be greater than the Galactic absorption in the direction of N4088–X1 (i.e., 2×10^{20} atoms cm^{-2}). The fit obtained, with a hard photon index of 1.3 (see Table 4), does not satisfactorily describe the observed spectrum, as two data points above 5 keV fall below the power-law fit (see Figure 3, top). We thus attempted to fit this spectrum with *wabs*diskbb* as with our *Chandra* data and an exponential cutoff *wabs*pow*highe*. Using the *wabs*diskbb* model, a fit with $\chi^2/\mathrm{dof} = 39.97/34$ and an inner disk temperature of 2.1 keV (see Table 4) is obtained. This temperature is again too high for optically thick emission from a typical optically thin accretion disk. A good fit ($\chi^2/\mathrm{dof} = 36.89/32$) is also obtained with the exponential cutoff model. The high-energy cutoff has also been observed in other ULXs (e.g., Dewangan et al. 2006, 2010; Stobbart et al. 2006; Roberts 2007; Gladstone et al. 2009; Sutton et al. 2013) and is well described by thermal Comptonization of hot coronal electrons by soft photons

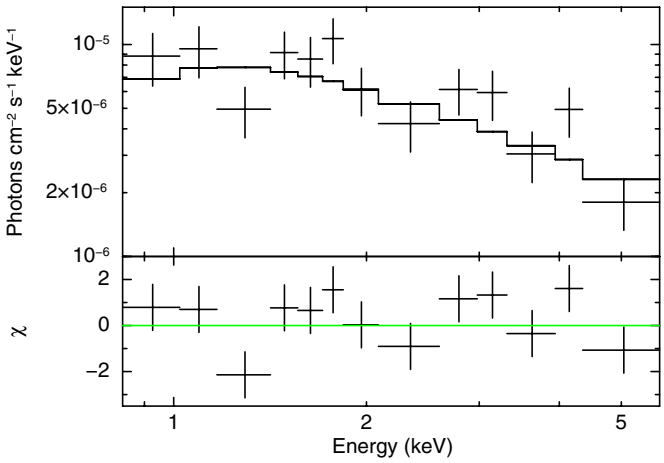

Figure 2. Power-law fit to the *Chandra* spectrum of N4088–X1.
(A color version of this figure is available in the online journal.)

Table 3
Spectral Parameters Obtained by Fitting the *Chandra* Spectrum with an Absorbed Power Law and Absorbed Disk-blackbody Model

Model	$N_{\rm H}$ (10^{22} cm^{-2})	$\Gamma/T_{\rm in}$ (/keV)	Norm.	Flux (erg cm^{-2} s^{-1})	χ^2/dof	p-value
pow	$0.3^{+0.5}_{-0.3}$	$1.1^{+0.6}_{-0.5}$	$(1.6^{+2}_{-0.7}) \times 10^{-5}$	$(1.7^{+0.6}_{-1.5}) \times 10^{-13}$	16.9/10	0.08
diskbb	$0.2^{+0.3}_{-0.2}$	$2.5^{+4}_{-0.9}$	2.1×10^{-4}	$(1.4^{+0.2}_{-1.4}) \times 10^{-13}$	15.62/10	0.11

Notes. The quoted flux is the observed flux in the 0.2 to 10 keV energy range. The errors provided are at 90% confidence level.

Table 4
Spectral Parameters Obtained by Fitting the *Swift* XRT Combined Spectrum of N4088–X1 with an Absorbed Power Law, Power Law with Exponential Cutoff, Disk-blackbody, and Thermal Comptonization Model

Model	$N_{\rm H}$ (10^{22} cm^{-2})	$\Gamma/T_{\rm in}$ (/keV)	Cutoff (keV)	T_0 (keV)	$kT_{\rm e}$ (keV)	τ	Norm.	Flux (erg cm^{-2} s^{-1})	χ^2/dof
pow	$0.05^{+0.06}_{-0.05}$	$1.3^{+0.2}_{-0.2}$	...	...	...	...	$(3.4^{+0.8}_{-0.6}) \times 10^{-5}$	$3.7^{+0.4}_{-0.3} \times 10^{-13}$	51.06/34
*pow*highe*	$0.02^{+0.03}_{-0.02}$	$0.9^{+0.2}_{-0.3}$	3^{+2}_{-1}	...	...	...	$(2.9^{+0.4}_{-0.3}) \times 10^{-5}$	$(3.0^{+0.4}_{-0.4}) \times 10^{-13}$	36.89/32
diskbb	$0.02^{+0.02}_{-0.02}$	$2.1^{+0.3}_{-0.4}$	...	...	...	...	$(8^{+7}_{-3}) \times 10^{-4}$	$(3.0^{+0.4}_{-0.3}) \times 10^{-13}$	39.97/34
comptt	$0.02^{+0.03}_{-0.02}$	...	...	$0.03^{+0.1}_{-0.03}$	$1.2^{+0.2}_{-0.2}$	17^{+3}_{-3}	$(1.3^{+1.0}_{-0.5}) \times 10^{-4}$	$(2.9^{+0.3}_{-0.3}) \times 10^{-13}$	35.01/32

Notes. The quoted flux is the observed flux in the 0.2 to 10.0 keV energy range. The errors provided are at 90% confidence level.

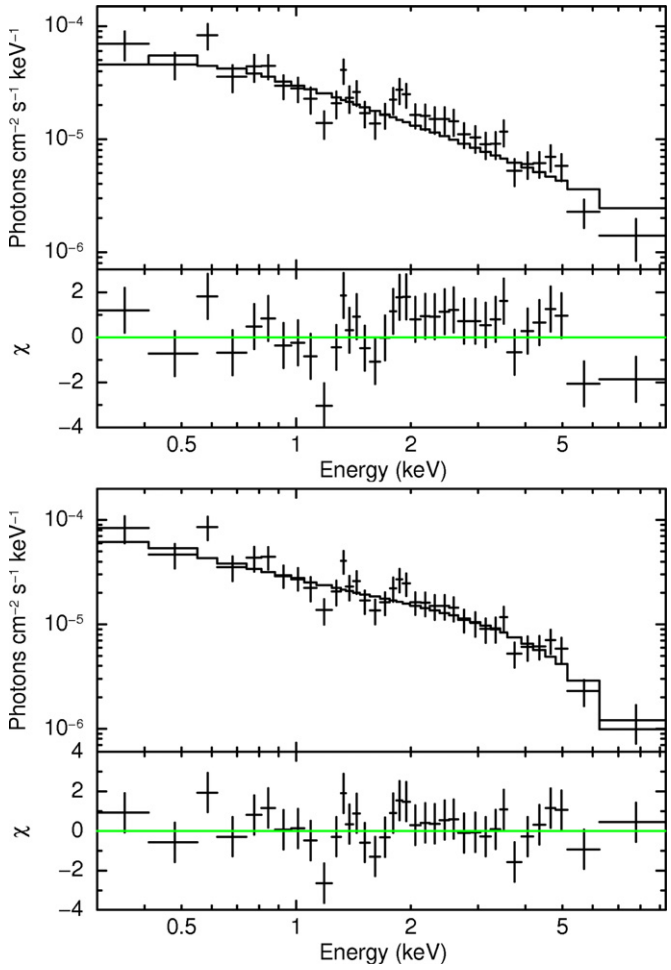

Figure 3. Fit to a power law (top) and a thermal Comptonization model (bottom) to the *Swift* XRT combined spectrum of N4088–X1.

(A color version of this figure is available in the online journal.)

(e.g., Titarchuk 1994; Hua & Titarchuk 1995). We thus test if a Comptonization model (*wabs*comptt*) is able to fit the data (Figure 3, bottom). We find that the *Swift* spectrum is well described (χ^2/dof = 35.01/32) with a Comptonization model of input soft photon temperature $T_0 < 0.1$ keV and plasma temperature $kT_{\rm e} = 1.2$ keV (see Table 4). The S/N is insufficient for us to detect any contribution from the disk, although the disk should still be present.

Both the *diskbb*, *pow*highe*, and *comptt* models provide significant improved statistics with respect to the *pow* model, as indicated by the χ^2/dof. The Bayesian Information Criterion (BIC; Schwarz 1978; Raftery 1995) can be also used as a further indicator of the statistical improvement of one model over another. The BIC value can be calculated as BIC $= 2\log(L_1) - 2\log(L_2) - (k_1 - k_2)\log(n)$, where $L = \exp(-\chi^2/2)$ for models 1 and 2, respectively, $k =$ number of parameters in model, and $n =$ number of data points. We obtain BIC values in the range 2–6 for the three models compared to the *pow* one, which is a "positive" result.[17] When comparing the *comptt* to the *diskbb* and *pow*highe* models, we obtain BIC numbers between 0 and 2, which indicate that the *comptt* is "preferred" over these models.

To quantify the significance of the spectral cutoff, we also try to fit a broken power law with the two slopes tied together and then thaw one of them and use the F-test to compare the fits. The F-test assesses whether the improvement of the χ^2 is due to chance or to the new component being significant (e.g., Barlow 1989). We obtain a break energy of $4.7^{+0.6}_{-0.9}$ keV, an F-statistic value of 6.04, and a probability of 0.006, which is $\ll 1$ and thus indicates that the cutoff is significantly there.

3.2. Radio Counterpart of the ULX

A 1.6 GHz radio counterpart to N4088–X1 consistent with the *ROSAT* X-ray detection was reported by Mezcua & Lobanov (2011). The *Chandra* position of N4088–X1 obtained here reveals an offset of 6 arcsec between the X-ray position and the 1.6 GHz EVN radio source of Mezcua & Lobanov (2011), which can now be ruled out as a candidate counterpart of the ULX.

The reanalysis of the 1.6 GHz using a FOV of 1 arcsec around the *Chandra* position yields the detection of compact

[17] The significance of a model over another is "preferred" for BIC values between 0–2, "positive" for BIC values between 2–6, "strong" for values 6–10, and "very" strong for BIC > 10.

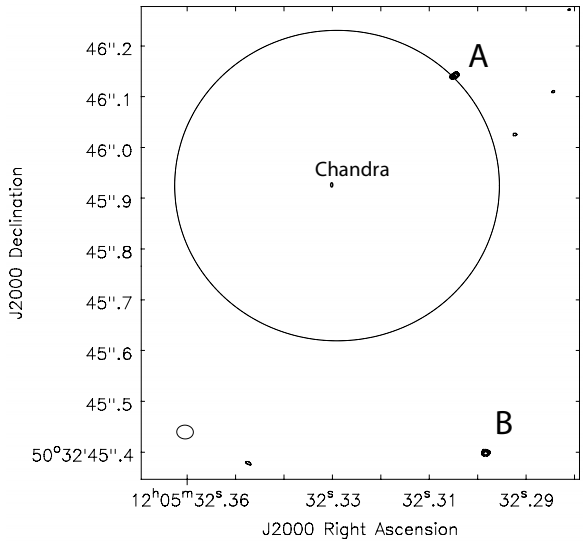

Figure 4. 1.6 GHz EVN image at the *Chandra* position of N4088–X1. The contours are (3, 4, 5) times the off-source rms noise of 11 μJy beam^{-1}. Two compact components labeled A and B are detected. A circle of radius 0.3 arcsec centered at the *Chandra* position is plotted to ease the visualization of the distance between the ULX and the radio components. The beam size shown at the bottom left corner is 33 mas × 27 mas oriented at a position angle of 86°.4.

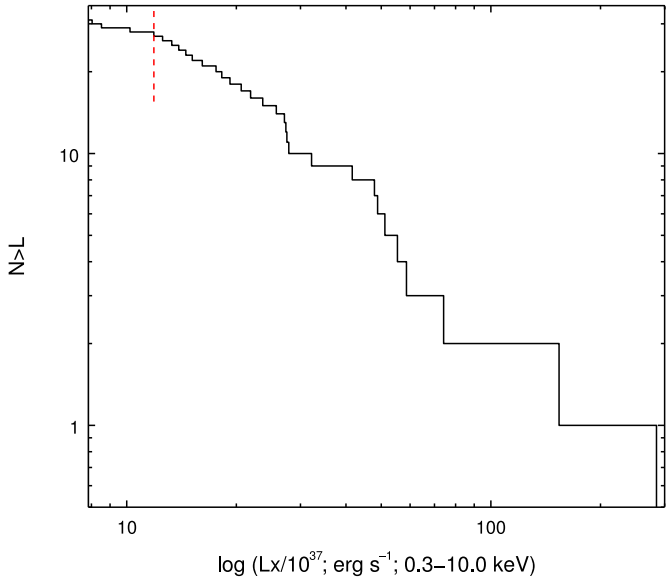

Figure 5. Cumulative XLF of NGC 4088. The vertical dotted red line shows the cut performed in the XLF to correct for incompleteness.
(A color version of this figure is available in the online journal.)

radio emission consistent, within 0.3 arcsec, with the *Chandra* positional error (component A in Figure 4). This compact component A is detected at a 5.2σ level and is centered at R.A.(J2000) = 12^{h}05^{m}32^s.3048 ± 0^s.0004, decl.(J2000) = 50°32′46″.140 ± 0″.004. It has an integrated flux density of 49 μJy, from which we derive a 1.6 GHz luminosity $L_{1.6\,\mathrm{GHz}} = 1.6\times10^{34}$ erg s^{-1}. The AIPS task JMFIT is used to fit an elliptical Gaussian to this peak of emission, which yields a lower limit on the brightness temperature $T_\mathrm{B} > 3 \times 10^4$ K.

A second component (labeled B in Figure 4) is detected at 5.4σ level offset 0.6 arcsec from the *Chandra* X-ray position. Component B is centered at R.A.(J2000) = 12^{h}05^{m}32^s.2983± 0^s.0003, decl.(J2000) = 50°32′45″.398 ± 0″.003, and has an integrated flux density of 55 μJy, from which we derive a 1.6 GHz luminosity $L_{1.6\,\mathrm{GHz}} = 1.8 \times 10^{34}$ erg s^{-1} assuming it is in NGC 4088. The fit of an elliptical Gaussian to this peak of emission yields a lower limit on the brightness temperature $T_\mathrm{B} > 3 \times 10^4$ K.

In the 5 GHz EVN observations, no radio emission is detected above a 5σ level for N4088–X1 within 1 arcsec of the *Chandra* position nor within a FOV of 5 arcsec around the VLA position. An upper limit on the flux density of the ULX of 0.30 mJy beam^{-1} is obtained by estimating the rms at the *Chandra* position, from which we derive an upper limit on the brightness temperature $T_\mathrm{B} < 6 \times 10^5$ K. Adopting a distance to NGC 4088 of 13 Mpc, we derive an upper limit on the 5 GHz radio luminosity of $L_{5\,\mathrm{GHz}} < 3.1 \times 10^{35}$ erg s^{-1}.

Combined with the 1.6 GHz detection, the upper limit on the flux density at 5 GHz can be used to constrain the spectral index of the source. Defining $F_\nu \propto \nu^\alpha$, we obtain $\alpha \leqslant 1.6$, which is trivially satisfied by any physical class of radio spectra. It should be noted that this spectral index is derived from non-simultaneous observations and can thus be affected by variability effects (unless changes in the radio emission occur on timescales longer than years). Therefore, deeper 5 GHz observations simultaneous with new 1.6 GHz ones are needed before we can determine the nature of the radio emission.

3.3. X-Ray Luminosity Function

3.3.1. AGN Fraction

In order to estimate the level of active galactic nucleus (AGN) contamination, we compared the flux distribution of the *Chandra* sources with the expected AGN flux distribution (Lehmer et al. 2012). We estimate that about 2/3 of the 31 *Chandra* sources detected inside the full S3 chip (area = 0.0196 deg^2) are likely to be AGN. However, for the 15 sources inside the D25 ellipse (area = 0.0028 deg^2), the AGN fraction is only ∼19% (i.e., ⩽3 AGN). In particular, the probability of finding an AGN inside the D25 with the flux measured for the ULX is ∼15%. Although the probability of detecting a background AGN inside the D25 of NGC 4088 is not very low, other considerations argue against this possibility for the ULX (see Section 4).

3.3.2. XLF Fitting

The XLF of the X-ray source population of NGC 4088 is constructed considering those sources inside the D25 ellipse of the galaxy. An apparent flattening of the XLF is observed at the low luminosities (see Figure 5), which may be caused by incompleteness effects. To correct for this, we eliminate the three lower points of the XLF that may be affected by incompleteness (it should be noted that the purpose of this paper is not to study the low-luminosity XLF of NGC 4088). As a result, the XLF flattening disappears.

Since the errors in the cumulative XLF are not independent, from now on we use the differential XLF. This allows us to take into account the statistical uncertainties, which are large given the very small number of sources. These errors do not take into account the possibility that ⩽3 sources inside the D25 are AGN.

We fit the differential XLF with a power law of the form $dN/dL_\mathrm{X} = BL_\mathrm{X}^{-\beta}$ normalized to 10^{37} erg s^{-1}, where $\beta = \alpha + 1$ (Figure 6). The Cash statistic (Cash 1979) is used instead of the minimum χ^2 method due to insufficient data points for the errors to be described by Gaussian statistics. The fit gives a slope of $\beta = 1.5 \pm 0.8$ (1σ error), and thus

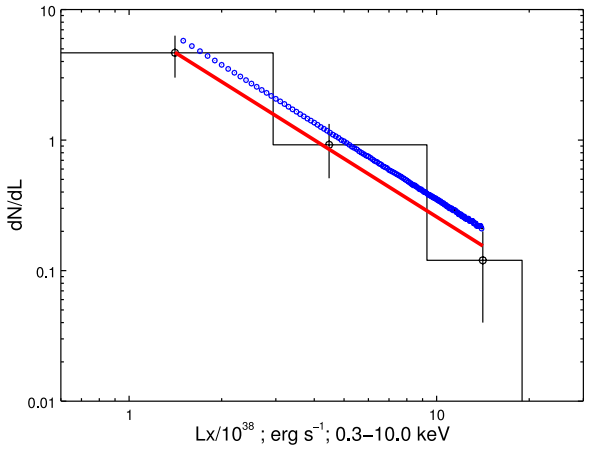

Figure 6. Fit of the differential XLF inside the D25 ellipse of NGC 4088 to a single power law (red solid line). The best-fit slope is $\alpha = 0.5 \pm 0.8$. The blue dotted line denotes the XLF of star-forming galaxies from Mineo et al. (2012) scaled by a factor 4.5.

(A color version of this figure is available in the online journal.)

$\alpha = 0.5 \pm 0.8$, which is similar to the slope found in other spiral galaxies (e.g., $\alpha \sim$ 0.4–0.5; the Antennae galaxies, Zezas & Fabbiano 2002; M82, Zezas et al. 2007; M81, Tennant et al. 2001). In these galaxies, the X-ray source population is mostly dominated by HMXBs. The ULX N4088–X1, with a luminosity $L_{0.2-10.0\,\mathrm{keV}} = 3.4 \times 10^{39}$ erg s^{-1}, could thus be located at the high end of the HMXB distribution of NGC 4088, which is consistent with the association of ULXs with young stellar populations (e.g., Zezas & Fabbiano 2002; Swartz et al. 2004). However, the possibility that the ULX is a LMXB (e.g., Middleton et al. 2012; Soria et al. 2012) cannot be ruled out.

To further study the star-formation rate (SFR) of NGC 4088, we overplot the XLF of star-forming galaxies from Mineo et al. (2012), Figure 4, therein, black line, on the XLF of NGC 4088. These authors normalize their XLF to 1 $M_\odot$ yr^{-1}. By rescaling this value to fit our data (see Figure 6), it is possible to obtain an estimate on the SFR for NGC 4088. This provides an estimated rate of 4.5 $M_\odot$ yr^{-1}, in good agreement with the range of SFRs 1.7–7.8 $M_\odot$ yr^{-1} obtained by Schmitt et al. (2006) in the Hα, IR, and radio bands.

3.4. The Supernova SN2009dd

Based on *Swift* XRT observations, Inserra et al. (2013) reported the X-ray detection of a recent Type II SN (SN2009dd) in the galaxy NGC 4088 at R.A.(J2000) = $12^{\mathrm{h}}05^{\mathrm{m}}34\overset{\mathrm{s}}{.}10$, decl.(J2000) = $50^\circ32'19\overset{''}{.}4$. SN2009dd brightened from 8×10^{38} erg s^{-1} to 1.7×10^{39} erg s^{-1} in the 0.2–10 keV energy range. While *XMM-Newton* does not have enough resolution to resolve the SN from the nucleus, the *Chandra* observations of NGC 4088 here presented can provide the most accurate X-ray position of SN2009dd.

In our *Chandra* observations, *wavdetect* fails to detect the SN2009dd. However, the source can be dimly seen in the 0.3–10 keV and 1.5–7.0 keV bands. Using CIAO Statistics, we obtain ∼8 counts in the 0.3–10 keV background subtracted image, which corresponds to an unabsorbed flux $F_{0.3-10\,\mathrm{keV}} = 4.2 \times 10^{-15}$ erg cm^{-2} s^{-1} and luminosity $L_{0.3-10\,\mathrm{keV}} = 8.4 \times 10^{37}$ erg s^{-1} assuming $\Gamma = 1.8$ and Galactic column density $N_{\mathrm{H}} = 2 \times 10^{20}$ cm^{-2}. From the detected number of source counts and background counts in the source extraction area, we can estimate the 90% confidence limit to the true number of counts coming from SN2009dd from Poisson statistics (e.g., Kraft et al. 1991). We obtain a 90% confidence level lower limit ∼3 and upper limit ∼13, which indicates that the source is real and not a background fluctuation. The chance probability of detecting ⩾8 counts for the given background is $\sim 10^{-5}$. The *Chandra* location of SN2009dd is R.A.(J2000) = $12^{\mathrm{h}}05^{\mathrm{m}}34\overset{\mathrm{s}}{.}08$, decl.(J2000) = $50^\circ32'19\overset{''}{.}0$, which is consistent with the *Swift* position within the ∼0.6 arcsec *Chandra* absolute astrometry.

No radio emission was detected at the position of SN2009dd above a 3σ upper limit of 0.35 mJy at 1.3 cm and of 0.15 mJy at 3.5 cm according to Stockdale et al. (2009), and there are no other recent observations of NGC 4088 apart from the ones reported in 2009. The VLBI observations presented in this paper are centered too far from the position of SN2009dd; hence, no further upper limits to the radio flux density can be provided.

4. DISCUSSION

The Nature of N4088–X1

The results of the XLF fitting (Section 3.3.2) show that the XLF of NGC 4088 is well described by a power law of $\alpha = 0.5$, which resembles the typical fits of HMXB XLFs and indicates that N4088–X1 could be located at the high-luminosity extension of the BH XRB distribution. These results are in agreement with studies of the XLF of star-forming galaxies (e.g., Grimm et al. 2003; Mineo et al. 2012) and of the location of ULXs in stellar clusters (e.g., Poutanen et al. 2013), which conclude that ULXs are a high-luminosity end of the XRB population harboring most possibly stellar-mass BHs rather than IMBHs.

When analyzing the *Chandra* X-ray spectrum of N4088–X1 (Section 3.1), we find that it is acceptably fitted both by a simple absorbed power-law continuum of $\Gamma = 1.1^{+0.6}_{-0.5}$ and by a disk-blackbody model with $kT_{\mathrm{in}} = 2.5$ keV. The hard power-law slope is consistent with the classification of N4088–X1 as a "hard ULX" (Soria 2011; Sutton et al. 2013). The physical interpretation of hard ULXs is still unclear: some authors (e.g., Winter et al. 2006) suggested that they are IMBHs in the low/hard state; others (e.g., Gladstone et al. 2009; Soria 2011; Sutton et al. 2013) explain them instead as one possible variety of super-Eddington accretion (e.g., Poutanen et al. 2007; King 2009). The photon index is much harder than the value of $\Gamma \sim 1.7$ that is typical of the low/hard state (e.g., Remillard & McClintock 2006) but consistent with it within the 90% margin of error, which does thus not rule out the interpretation of N4088–X1 as an IMBH. A disk temperature >1 keV is however not consistent with an IMBH but favors the nature of N4088–X1 as an XRB with super-Eddington accretion. The low number of detected counts are insufficient to statistically distinguish between the models.

In the spectral fitting performed on the *Swift* data, a disk-blackbody model with $kT_{\mathrm{in}} \sim 2$ keV provided a better fit than the power-law model. A hint of a spectral cutoff at ∼5 keV seems to be observed in the residuals of the power-law model. This feature is similar to that observed in other ULXs (e.g., Dewangan et al. 2006, 2010; Stobbart et al. 2006; Kajava et al. 2012; Sutton et al. 2013), suggesting that N4088–X1 could be in the ultraluminous state (e.g., Roberts 2007; Gladstone et al. 2009; Kajava & Poutanen 2009; Sutton et al. 2013) with a thermal spectrum described by Compton scattering of soft photons (e.g., Middleton et al. 2012; Soria et al. 2012; Straub et al. 2013). The good fit provided by the thermal Comptonization model together with the statistically significant cutoff indicated by the *F*-test support this possibility, although the *Swift* data are

not of high enough S/N to confirm it. Therefore, while the spectrum is merely quasi-thermal in shape, we are unable to confirm the accretion state at this time using the X-ray data at hand. However, we can place constraints on the nature of N4088–X1 when combining these fits with information from other wavebands.

In Section 3.2 we have reported the 1.6 GHz EVN detection of two compact components within the *Chandra* error circle of 0.6 arcsec. These could be either compact H II regions (e.g., see review by Churchwell 2002), compact supernova remnants (SNRs), or an accreting BH. Compact H II regions have typical sizes of 1–7 pc, a thermal X-ray spectrum with temperatures >2 keV, an inverted radio spectrum of spectral index ∼1, and $T_{\rm B} < 10^4$ K (e.g., Johnson et al. 2001; McDonald et al. 2002; Tsujimoto et al. 2006; Hoare et al. 2007). Compact SNRs have also typical sizes of a few pc and a steep radio spectrum (e.g., Lacey et al. 2007; Mezcua et al. 2013b). The limits on the brightness temperatures derived from the 1.6 GHz detections and the 5 GHz non-detection ($3 \times 10^4 < T_{\rm B} < 6 \times 10^5$ K) together with the high X-ray luminosity of N4088–X1 make the presence of compact H II regions quite improbable and are more indicative of the presence of either compact SNRs or an accreting BH. The EVN beam size of ∼30 mas (which corresponds to ∼2 pc at the distance of the galaxy) is consistent with both a compact H II region, a compact SNR, and an accreting BH. Unfortunately, the non-detection at 5 GHz and the upper limit on the radio spectral index ($\alpha \leqslant 1.6$) estimated for N4088–X1 does not clarify whether the radio counterpart of this ULX is steep, flat, inverted, or variable. We plan to obtain deeper radio observations to determine the spectral index and variability properties of this source and therefore constrain the physical interpretation.

In order to test if the two radio components are associated with the ULX, we derive the probability of a chance alignment between the *Chandra* counterpart and any compact radio source in the 5 arcsec field (positional error of the VLA) in that region of the galaxy. We use the number of sources detected above 5σ in the imaged VLA field (see Section 2.3) and the *Chandra* error circle of 0.6 arcsec following the same approach as in Mezcua et al. (2013a). This gives a probability of chance alignment $P(\mathrm{CA}) = 0.4$, which is quite high and indicates that one or the two detected compact radio components (A and B, Figure 4) could correspond to a random source (i.e., a compact SNR or BH) not associated with the ULX. Given the 0.6 arcsec offset between component B and the *Chandra* position, component B is most plausibly not related to N4088–X1 while the radio emission of component A (consistent with the *Chandra* position within 0.3 arcsec) could be coming from a BH associated with the ULX. In this case, the emission of component A could be due to flaring radio emission from a ballistic jet (e.g., Webb et al. 2012; Middleton et al. 2013) or compact core emission if the source is in a low/hard state (albeit, as mentioned above, with a flatter photon spectral index than typical). The results of the X-ray spectral analysis suggest that N4088–X1 is in a thermal (i.e., Comptonized) ultraluminous state. Therefore, if the radio emission is associated with the ULX then the compact radio component is most likely associated with ballistic jet emission.

If we assume for a moment that the source is residing in the low/hard state accreting at $L < 10\%$ Eddington (e.g., Done & Gierliński 2003), we are able to invoke the fundamental plane of accreting BHs (e.g., Merloni et al. 2003; Körding et al. 2006; Gallo et al. 2012) and estimate a BH mass. For this, we use the 2–10 keV X-ray flux obtained from the *Chandra* spectral fitting and scale the 1.6 GHz flux density to 5 GHz using a radio spectral index $\alpha = 0.15$ (a typical spectral index for flat cores used to estimate the BH mass from the Fundamental Plane, e.g., Falcke et al. 2004). Using the Fundamental Plane of Körding et al. (2006) that presents the least scatter, an upper limit on the BH mass of $3 \times 10^5\ M_\odot$ is obtained. This is consistent with this source being either an IMBH or an XRB, and rules out the nature of N4088–X1 as an SMBH.

We also derive the ratio $R_{\rm X}$ of 5 GHz radio emission to 2–10 keV X-ray emission defined by Terashima & Wilson (2003). Typical values of this ratio for XRBs are $R_{\rm X} < -5.3$ (e.g., Reines et al. 2011), while values of $R_{\rm X} = -2.7$ to -2 have been estimated in SNRs (e.g., Neff et al. 2003; Mezcua et al. 2013b). For low-luminosity AGN (LLAGN), Ho (2008) reports a range of values $-3.8 < R_{\rm X} < -2.8$ (see also Mezcua et al. 2013a, Table 3). For N4088–X1, we obtain $R_{\rm X} < -4.7$ using the 2–10 keV X-ray flux obtained from the *Chandra* spectral fitting and the 5 GHz- scaled radio luminosity. This is in agreement with the previous results, ruling out both an SMBH and an SNR nature for this ULX.

The location of N4088–X1 in the spiral arm of the host galaxy, possibly within an H II region (e.g., Sánchez-Sutil et al. 2006), and the low X-ray absorption seen in the *Chandra* and *Swift* data also argue very strongly against a LLAGN background scenario. On the other hand, the lack of a bright counterpart to N4088–X1 in the optical image makes it very unlikely to be a foreground star.

5. CONCLUSIONS

We have presented the first *Chandra* and *Swift* X-ray observations of the galaxy NGC 4088 and the ULX N4088–X1 that it hosts. EVN observations at 1.6 and 5 GHz of the ULX were performed almost simultaneously with the *Swift* and *Chandra* observations, respectively, which have allowed us to investigate the compact radio emission of a ULX radio counterpart previously proposed with the VLA.

The X-ray spectral analysis of N4088–X1 seems to favor a thermally Comptonized spectrum for this source, although the possibility that it is a hard ULX cannot be ruled out. The disk temperature ($kT_{\rm in} \sim 2$ keV) obtained from the disk-blackbody model and the presence of a statistically significant spectral break at ∼5 keV are not consistent with N4088–X1 being an IMBH but suggest that the source could be an XRB in a super-Eddington ultraluminous state. Unfortunately, this cannot be confirmed with the present data due to the low S/N. If the source is in an ultraluminous state, the detection of compact radio emission at 1.6 GHz coincident with the *Chandra* counterpart could then correspond to ballistic jet emission from an accreting BH. Multi-epoch multi-wavelength observations are required to confirm this.

Finally, the detection of 15 sources within the D25 ellipse of NGC 4088 has allowed us to fit the XLF of this galaxy and estimate an SFR of 4.5 $M_\odot\ \mathrm{yr}^{-1}$. We find that the XLF resembles that of typical star-forming galaxies, where the ULX N4088–X1 could be at the high-luminosity end of the XRB population. We thus conclude that N4088–X1 is possibly an HMXB with a thermally Comptonized spectrum and either approaching the Eddington limit or in the ultraluminous state.

This work was partially supported by the Chandra X-Ray Center (CXC), which is operated by the Smithsonian

Astrophysical Observatory (SAO) under NASA contract NAS8-03060, and by Chandra Director Discretionary Time grant DD2-13063X. M.M. acknowledges financial support from AYA2011-25527. J.C.G. would like to acknowledge Avadh Bhatia Fellowship, the Alberta Ingenuity New Faculty Award, and the financial support from NSERC Discovery Grants. S.A.F. is the recipient of an Australian Research Council Postdoctoral Fellowship, funded by grant DP110102889. RS acknowledges support from the Australian Research Council's Discovery Projects funding scheme (project number DP120102393).

REFERENCES

Arnaud, K. A. 1996, in ASP Conf. Ser. 101, Astronomical Data Analysis Software and Systems V, ed. G. H. Jacoby & J. Barnes (San Francisco, CA: ASP), 17
Bachetti, M., Rana, V., Walton, D. J., et al. 2013, ApJ, 778, 163
Barlow, R. 1989, Statistics. A Guide to the Use of Statistical Methods in the Physical Sciences (Manchester Physics Series) (reprint ed.; New York: Wiley)
Belczynski, K., Bulik, T., Fryer, C. L., et al. 2010, ApJ, 714, 1217
Boroson, B., Kim, D.-W., & Fabbiano, G. 2011, ApJ, 729, 12
Caballero-García, M. D., Belloni, T., & Zampieri, L. 2013, MNRAS, 436, 3262
Caballero-García, M. D., & Fabian, A. C. 2010, MNRAS, 402, 2559
Cash, W. 1979, ApJ, 228, 939
Churchwell, E. 2002, ARA&A, 40, 27
Colbert, E. J. M., Heckman, T. M., Ptak, A. F., Strickland, D. K., & Weaver, K. A. 2004, ApJ, 602, 231
Colbert, E. J. M., & Mushotzky, R. F. 1999, ApJ, 519, 89
Cseh, D., Grisé, F., Corbel, S., & Kaaret, P. 2011, ApJL, 728, L5
Cseh, D., Lang, C., Corbel, S., Kaaret, P., & Grisé, F. 2011, in IAU Symp. 275, Jets at all Scales, ed. G. E. Romero, R. A. Sunyaev, & T. Belloni (Cambridge: Cambridge Univ. Press), 325
Davis, S. W., Narayan, R., Zhu, Y., et al. 2011, ApJ, 734, 111
De Marco, B., Ponti, G., Miniutti, G., et al. 2013, MNRAS, 436, 3782
Dewangan, G. C., Griffiths, R. E., & Rao, A. R. 2006, ApJL, 641, L125
Dewangan, G. C., Misra, R., Rao, A. R., & Griffiths, R. E. 2010, MNRAS, 407, 291
Done, C., & Gierliński, M. 2003, MNRAS, 342, 1041
Evans, P. A., Beardmore, A. P., Page, K. L., et al. 2009, MNRAS, 397, 1177
Fabbiano, G. 1989, ARA&A, 27, 87
Fabbiano, G. 2005, Sci, 307, 533
Fabbiano, G. 2006, ARA&A, 44, 323
Falcke, H., Körding, E., & Markoff, S. 2004, A&A, 414, 895
Feng, H., & Soria, R. 2011, NewAR, 55, 166
Gallo, E., Miller, B. P., & Fender, R. 2012, MNRAS, 423, 590
Garmire, G. P. 1997, BAAS, 29, 823
Gilfanov, M. 2004, MNRAS, 349, 146
Gladstone, J. C., Copperwheat, C., Heinke, C. O., et al. 2013, ApJS, 206, 14
Gladstone, J. C., & Roberts, T. P. 2009, MNRAS, 397, 124
Gladstone, J. C., Roberts, T. P., & Done, C. 2009, MNRAS, 397, 1836
Godet, O., Plazolles, B., Kawaguchi, T., et al. 2012, ApJ, 752, 34
Grimm, H.-J., Gilfanov, M., & Sunyaev, R. 2003, MNRAS, 339, 793
Heger, A., Fryer, C. L., Woosley, S. E., Langer, N., & Hartmann, D. H. 2003, ApJ, 591, 288
Heil, L. M., Vaughan, S., & Roberts, T. P. 2009, MNRAS, 397, 1061
Ho, L. C. 2008, ARA&A, 46, 475
Hoare, M. G., Kurtz, S. E., Lizano, S., Keto, E., & Hofner, P. 2007, Protostars and Planets V, Vol. 951 (Tucson, AZ: Univ. Arizona Press), 181
Hua, X.-M., & Titarchuk, L. 1995, ApJ, 449, 188
Inserra, C., Pastorello, A., Turatto, M., et al. 2013, A&A, 555, A142
Johnson, K. E., Kobulnicky, H. A., Massey, P., & Conti, P. S. 2001, ApJ, 559, 864
Kaaret, P., & Corbel, S. 2009, ApJ, 697, 950
Kajava, J. J. E., & Poutanen, J. 2009, MNRAS, 398, 1450
Kajava, J. J. E., Poutanen, J., Farrell, S. A., Grisé, F., & Kaaret, P. 2012, MNRAS, 422, 990
Kalberla, P. M. W. 2003, ApJ, 588, 805
Kim, D.-W., & Fabbiano, G. 2004, ApJ, 611, 846
Kim, D.-W., & Fabbiano, G. 2010, ApJ, 721, 1523
King, A. R. 2009, MNRAS, 393, L41
King, A. R., Davies, M. B., Ward, M. J., Fabbiano, G., & Elvis, M. 2001, ApJL, 552, L109
Körding, E., Falcke, H., & Corbel, S. 2006, A&A, 456, 439
Kraft, R. P., Burrows, D. N., & Nousek, J. A. 1991, ApJ, 374, 344
Lacey, C. K., Goss, W. M., & Mizouni, L. K. 2007, AJ, 133, 2156
Lasker, B. M., Sturch, C. R., McLean, B. J., et al. 1990, AJ, 99, 2019
Lehmer, B. D., Xue, Y. Q., Brandt, W. N., et al. 2012, ApJ, 752, 46
Liu, J.-F., & Bregman, J. N. 2005, ApJS, 157, 59
Mapelli, M., Ripamonti, E., Zampieri, L., Colpi, M., & Bressan, A. 2010, MNRAS, 408, 234
McClintock, J. E., & Remillard, R. A. 2006, Black Hole Binaries (Cambridge: Cambridge Univ. Press), 157
McDonald, A. R., Muxlow, T. W. B., Wills, K. A., Pedlar, A., & Beswick, R. J. 2002, MNRAS, 334, 912
Merloni, A., Heinz, S., & di Matteo, T. 2003, MNRAS, 345, 1057
Mezcua, M., Farrell, S. A., Gladstone, J. C., & Lobanov, A. P. 2013a, MNRAS, 436, 1546
Mezcua, M., & Lobanov, A. P. 2011, AN, 332, 379
Mezcua, M., Lobanov, A. P., & Martí-Vidal, I. 2013b, MNRAS, 436, 2454
Mezcua, M., Roberts, T. P., Sutton, A. D., & Lobanov, A. P. 2013c, MNRAS, 436, 3128
Middleton, M. J., Miller-Jones, J. C. A., Markoff, S., et al. 2013, Natur, 493, 187
Middleton, M. J., Sutton, A. D., Roberts, T. P., Jackson, F. E., & Done, C. 2012, MNRAS, 420, 2969
Miller, J. M., Fabbiano, G., Miller, M. C., & Fabian, A. C. 2003, ApJL, 585, L37
Mineo, S., Gilfanov, M., & Sunyaev, R. 2012, MNRAS, 419, 2095
Neff, S. G., Ulvestad, J. S., & Campion, S. D. 2003, ApJ, 599, 1043
Pakull, M. W., Grisé, F., & Motch, C. 2006, in IAU Symp. 230, Populations of High Energy Sources in Galaxies, ed. E. J. A. Meurs & G. Fabbiano (Cambridge: Cambridge Univ. Press), 293
Poutanen, J., Fabrika, S., Valeev, A. F., Sholukhova, O., & Greiner, J. 2013, MNRAS, 432, 506
Poutanen, J., Lipunova, G., Fabrika, S., Butkevich, A. G., & Abolmasov, P. 2007, MNRAS, 377, 1187
Raftery, R. E. K.. A. E. 1995, J. Am. Stat. Associat., 90, 773
Reines, A. E., Sivakoff, G. R., Johnson, K. E., & Brogan, C. L. 2011, Natur, 470, 66
Remillard, R. A., & McClintock, J. E. 2006, ARA&A, 44, 49
Roberts, T. P. 2007, Ap&SS, 311, 203
Sánchez-Sutil, J. R., Muñoz-Arjonilla, A. J., Martí, J., et al. 2006, A&A, 452, 739
Sarazin, C. L., Irwin, J. A., & Bregman, J. N. 2000, ApJL, 544, L101
Sarazin, C. L., Irwin, J. A., & Bregman, J. N. 2001, ApJ, 556, 533
Schmitt, H. R., Calzetti, D., Armus, L., et al. 2006, ApJ, 643, 173
Schwarz, G. 1978, AnSta, 5, 461
Servillat, M., Farrell, S. A., Lin, D., et al. 2011, ApJ, 743, 6
Soria, R. 2011, AN, 332, 330
Soria, R., Kuntz, K. D., Winkler, P. F., et al. 2012, ApJ, 750, 152
Soria, R., Motch, C., Read, A. M., & Stevens, I. R. 2004, A&A, 423, 955
Stobbart, A.-M., Roberts, T. P., & Wilms, J. 2006, MNRAS, 368, 397
Stockdale, C. J., Weiler, K. W., Immler, S., et al. 2009, ATel, 2016, 1
Strateva, I. V., & Komossa, S. 2009, ApJ, 692, 443
Straub, O., Done, C., & Middleton, M. 2013, A&A, 553, A61
Strohmayer, T. E., & Mushotzky, R. F. 2003, ApJL, 586, L61
Strohmayer, T. E., Mushotzky, R. F., Winter, L., et al. 2007, ApJ, 660, 580
Sutton, A. D., Roberts, T. P., & Middleton, M. J. 2013, MNRAS, 435, 1758
Swartz, D. A., Ghosh, K. K., Tennant, A. F., & Wu, K. 2004, ApJS, 154, 519
Swartz, D. A., Soria, R., Tennant, A. F., & Yukita, M. 2011, ApJ, 741, 49
Swartz, D. A., Tennant, A. F., & Soria, R. 2009, ApJ, 703, 159
Tao, L., Feng, H., Grisé, F., & Kaaret, P. 2011, ApJ, 737, 81
Tennant, A. F., Wu, K., Ghosh, K. K., Kolodziejczak, J. J., & Swartz, D. A. 2001, ApJL, 549, L43
Terashima, Y., & Wilson, A. S. 2003, ApJ, 583, 145
Titarchuk, L. 1994, ApJ, 434, 570
Tsujimoto, M., Hosokawa, T., Feigelson, E. D., Getman, K. V., & Broos, P. S. 2006, ApJ, 653, 409
Verheijen, M. A. W., & Sancisi, R. 2001, A&A, 370, 765
Webb, N., Cseh, D., Lenc, E., et al. 2012, Sci, 337, 554
Weisskopf, M. C., Brinkman, B., Canizares, C., et al. 2002, PASP, 114, 1
Winter, L. M., Mushotzky, R. F., & Reynolds, C. S. 2006, ApJ, 649, 730
Zampieri, L., & Roberts, T. P. 2009, MNRAS, 400, 677
Zezas, A., & Fabbiano, G. 2002, ApJ, 577, 726
Zezas, A., Fabbiano, G., Baldi, A., et al. 2007, ApJ, 661, 135